

Deep Learning for the Climate-Exhumation relationships of the of the Andes Mountains

Henry Crawford
EOSC 543: Basin Analysis

Abstract

The Andes mountains are extensive range that extends the length of South America. Thus, varying climatic conditions and atmospheric circulation within the southern hemisphere interact diversely across the latitudinal gradient of the cordillera. Reasonably, we would expect strong interactions between climatic conditions and surface geomorphology. However, further analysis show first-order climatic influence on the tectonic processes responsible for orogeny of this system and ultimate topographic expression. Deep-learning was applied to existing geologic and environmental datasets to successfully predict rates of exhumation from 0 to 2 Ma across the Central Andes. A low model RMSE of 0.073 km/Ma allowed for confident extrapolation of the model to the extent of the Andes, from 10°N to 50°S. Analysis of predicted exhumation, regional climate, and denudation with tectonics provide valuable insight to the climate control on Andean orogenic processes. This includes estimates of surface uplift, and migration of the orogen into the foreland due to precipitation-limited rates of exhumation and denudation in arid regions of the Andes.

Introduction

The Andes Mountains are an extensive series of transverse mountain ranges, or cordilleras, which extend down the west coast of South America. The orogen is a result of convergence between the Nazca tectonic plate to the west and the South American plate to the east. The Andean subduction margin and resulting orogen has evolved complexly through time and space, however, is generally characterized by a plunging oceanic slab and crustal shortening of the overriding continental plate. Crustal thickening is considered to be the result of a back-arc thrust wedge from the east of the orogen. The product is extraordinarily tall peaks, and the longest mountain range in the world.

High elevation areas are a source of detrital material for basins on both sides of the Andes. The amount of eroded material available is an inherent function of both tectonic, and climatic conditions (Garner 1959). *Denudation* can be considered as the amount of material *removed* at the earth surface at any given point, driven by processes of uplift, relief, erosion and topographic expression (Ahnert, 1970; Ring et al., 1999). Most of this material is transported to lower elevation accommodation space i.e. basins as suspended sediment in waterways (Garner, 1959), though high topographic relief can enable sediment transport by mass wasting events such as landslides and rock avalanches. *Exhumation* can be considered the vertical distance traveled by a particular rock in relation to earth's surface. The rate of exhumation is integrated with differences in rock and surface velocity (i.e. uplift) along its material path (Ring et al., 1999) and is known to increase with geothermal gradient (Stadler et al, 2020). Exhumation has been traditionally measured by thermochronology analyses which takes advantage of mineral cooling depths and geochemical rates of radioactive decay to determine distance traveled over a particular length of time (Fox et al., 2013). Ultimately, rates of exhumation are a function of rock uplift, geothermal gradient, and exposure by faulting, but also surface erosion. While inherently linked, denudation rates can differ significantly from exhumation rates provided varying erosional

conditions like relief, lithology, and climate (Ring et al., 1999).

The Andes mountains are positioned as a noteworthy barrier to global atmospheric circulation and moisture in the southern hemisphere (Xu et al., 2004), and continental precipitation patterns are primarily driven by Hadley cell precipitation regimes and global-scale atmospheric circulation systems (Montgomery et al., 2001). To a lesser degree, orographic lift produces increased moisture along the windward margins of the mountain range. However, this effect is localized and diminishes as overall moisture availability decreases to the south with decreasing strength of the Intertropical Convergence Zone (ITCZ) and South American Monsoon (Espinoza et al., 2020). A low-pressure belt and seasonal shifts in the westerlies bring cold moisture to the Andes most southern extent (Compagnucci, 2011). Evidently, we would expect strong relations between tectonic expression and climate as varying levels of precipitation, glaciation, and temperature work to erode mountain systems. While tectonic processes fundamentally drive the formation of the Andes at large, climate-erosion feedbacks also play a meaningful role in shaping topographic expression and have first order control on the orogenic process (e.g., Strecker et al., 2007; Stadler et al., 2020; Lamb and Davis, 2003; Montgomery et al., 2001; Compagnucci, 2011).

This research aims to take advantage of the strong relationships between climate and tectonics to model rates of exhumation over the last 0 to 2 Ma across the Andes. This work 1) finds that rates of exhumation, as typically measured by thermochronology analyses, can be predicted using widely available environmental datasets, 2) uses this model to predict exhumation across the Andes, and 3) examines preliminary relationships between modeled exhumation and regional tectonic setting and expression.

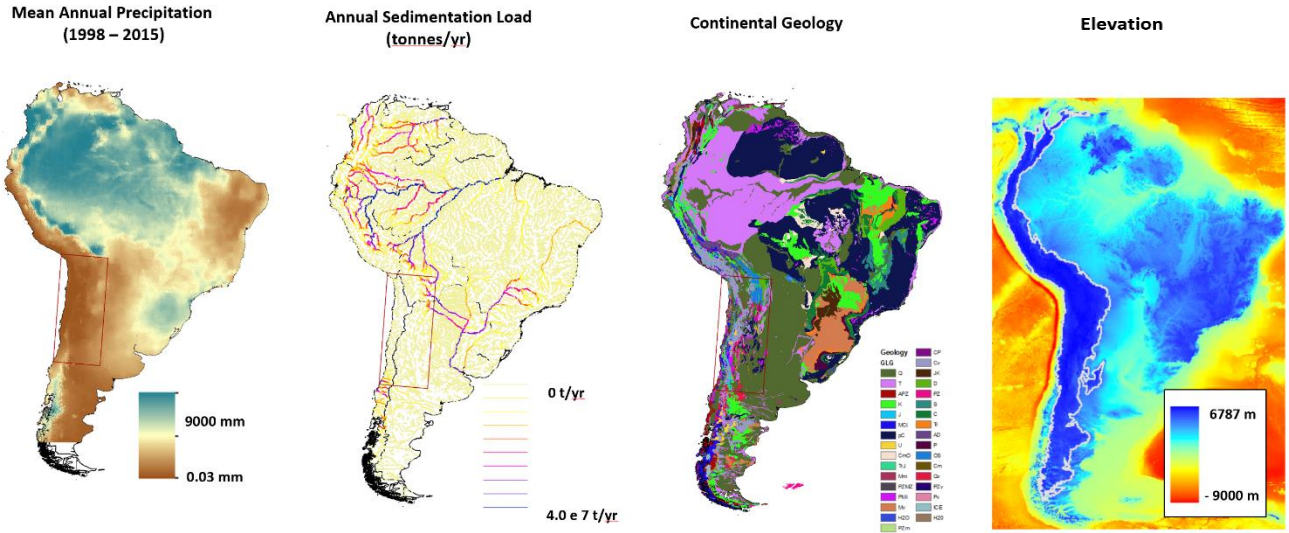


Figure 1. South America datasets. Region of Interest (ROI) used to train the MLP model shown as a red box. Geology legend from USGS (1999) is shown in Appendix A. The white line plotted over the elevation dataset (right) traces a 1000 m contour, representing the extend of the high elevation Andes mountains used in this study.

2. Methods

2.1 Dataset Pre-processing

Several datasets were sourced for this work: 1) exhumation rates of the Central Andes compiled and calculated from thermochronology analysis by Stalder et al., (2020) for the time period from 0 – 2 Ma, 2) hydrologic data of sedimentation load and catchment area calculated by Fagundes et al., (2020) for South

American river basins, 3) precipitation data from the Tropical Rainfall Measuring Mission (TRMM) satellite (NASA, 2018), 4) a digitized geologic map of South America (USGS, 1999), and 5) 15 arc-second resolution topography-bathymetry data (GEBCO, 2021) (Figure 1). It should be noted that this study assumes contemporary observations of precipitation, sedimentation load, and mapped geology when training and modeling rates of exhumation over the last 0 – 2 Ma.

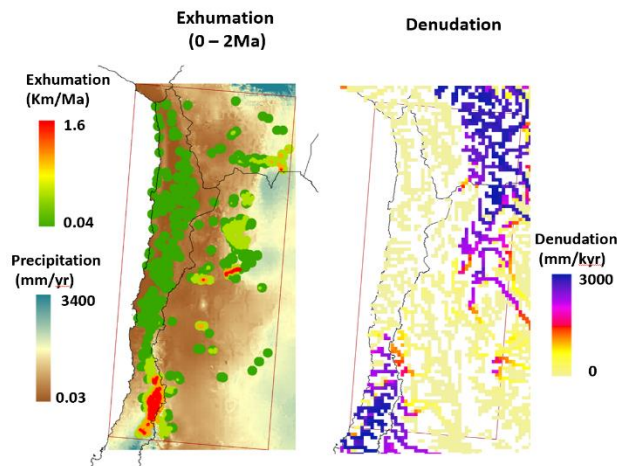


Figure 2. Region of Interest. Raw exhumation rates within the region of interest used to train the MLP model (Stalder et al., 2020), plotted over mean annual precipitation from 1998-2015 (left). Calculated denudation rates from annual sediment load and catchment area values, computed across the Andes, and shown in the ROI (right).

Denudation rates were calculated by first converting sedimentation load (Figure 1) into material volume using an average density of 2.65 t/m^3 , and then dividing by area of the draining basin from which the sediments were derived (*e.g.*, Fagundes et al., 2020; Morris and Fan, 1998). Results are average rates of lowering of the land surface (Figure 2). This was computed across the Andes mountains where data was available (Figure 1). Though, denudation measurements were attributed to the river channel locations as catchment area boundaries were not available in this study.

All datasets, except exhumation, were converted into raster format for sampling using ArcMap Desktop software (v.10.8.1). Nearest-neighbor interpolation methods were used for geologic unit and sediment supply rasterization, and bilinear interpolation for

denudation to slightly smooth the calculations within catchment basins. Pixel ground-sampling-distance was kept at the spatial extent of the vector polygon or point layer. This limits the possible extent of overlap between dataset observations, but also avoids false interpolations across catchment, basin, and fault boundaries. Next, the raster datasets were sampled within our region of interest (ROI), at each spatial location containing an exhumation rate ($n = 92,586$) (Figure 2). The ROI is the extent of thermochronology-derived exhumation data available in for this study. Only locations containing a value from each dataset (exhumation, precipitation, denudation, sediment load, and geology) were kept for further analysis ($n = 5,374$) (see Figure 7).

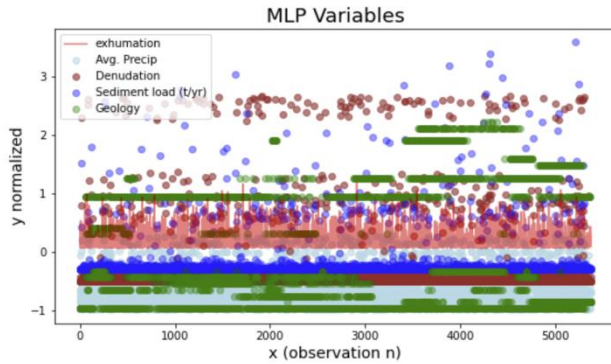


Figure 3. Normalized spread of variables used to develop the MLP machine-learning model.

2.2. Modeled Exhumation

Python 3.9 was used to develop a Multi-layer Perceptron regressor (MLP) set to train, validate, and test the prediction of *exhumation* (y) from input variables *precipitation*, *denudation*, *sediment load*, and *geology* (x_1, \dots, x_4) (Figure 3). The MLP regressor is a machine-learning algorithm which uses a series of input neurons (x_1, \dots, x_4) to predict output neuron values (y) by a series of hidden-layers and hidden-neuron connections. Each neuron pathway provides unique parametrization and weighting (Figure 4). All input variables were normalized between 0 and 1 to remove weighting bias and neuron saturation by large values with different scales. Exhumation rates were kept within their observed scale (~ 0 to 1.2) to maintain physical units as predicted output, which is reasonable given the closeness to the 0 to 1, and use of the linear ReLu activation function. The model was trained on a

subset of training data (65%), which was then validated internally (15%) within the neural-network structure to reduce the *loss* or *error* between actual and predicted y values. Final predicted exhumation (y) values were then *tested* on a subset of the original dataset (20%) completely independent of training and validation. The MLP model initiates with random starting parametrization values, and thus, the optimal number of hidden layers and neurons may change between model runs. A model ensemble was built to yield the most robust predictor of exhumation. The MLP regressor was iteratively run under 888 unique hyperparameters, with the number of hidden neurons ranging from 1 to 8, and number of hidden-neurons within each layer ranging from 1 to 11 (Figure 4). This iteration was completed for 10 model runs, each with unique and random initial parametrization of variables. The Root Mean Square Error (RMSE) between observed and predicted exhumation of the independent testing dataset were calculated for each model iteration. The ten models with the lowest RMSE were used to form the model ensemble (Figures 5 and 6). Model hyperparameters can be found in the supplementary code provided, but of note is the 'Relu' activation which was used to linearly trigger positive y predictions regardless of their closeness to the minimum or maximum value, and the regularization parameter ($\alpha = 0.01$) used to penalize variables with high weights and prevent overfitting of the model.

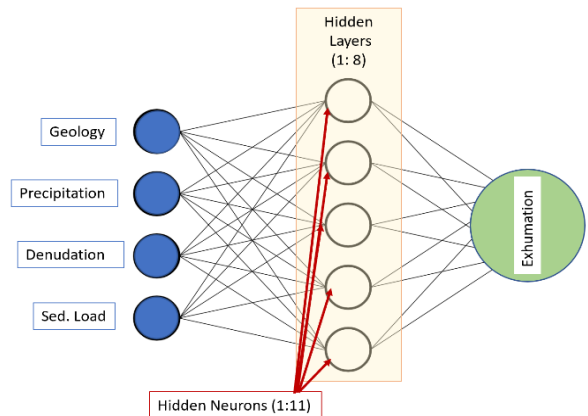


Figure 4. Multi-layer Perceptron regressor (MLP) machine-learning model structure, as developed for this study (schematic adapted from UBC EOSC510).

Next, a 1000 m contour interval was produced from the GEBCO (2021) 15 arc-second elevation dataset (Figure 1). This polygon is representative of the Andes mountains extent from 10°N to 50°S. Each of the raster datasets were clipped to the 1000 m contour interval. A 100 x 100 m grid of vector points was generated within this contour interval. The input variables *precipitation, denudation, sediment load, and geology* were sampled at each grid location and locations with incomplete data observations were dropped. The new data was input into the trained MLP and used to predict rates of exhumation across the Andes mountains ($n = 48,376$) (Figure 8).

2.3. Geologic- Climatic Analysis

Results from the orogen-wide modeled exhumation rates, and accompanying environmental datasets, were analyzed for relationships between tectonics and climate through a series of analytical plots (Figures 8 – 13). The width of the orogen at the 1000 m elevation-contour was calculated at 1-degree latitudinal intervals from 10°N to 50°S. This was done by differencing the maximum and minimum longitudes within each latitudinal step and converting the difference from degrees to kilometers (1° longitude = 113.3 km). These measurements are considered orthogonal to strike of the subduction considering the largely north/south direction of the Andes. Additionally, average values for all variables were calculated within each latitudinal step.

Results

The MLP machine-learning model successfully estimated rates of exhumation against testing data in our ROI (Figures 5 - 7). This is validated by a RMSE of 0.073 km/Ma of the model ensemble. Considering an output range from 0 – 1.2, this represents roughly a 6.1% spread between predicted values from the model and the actual values in the dataset. However, the model does appear to underpredict exhumation around 0.2 and 0.5 km/Ma (Figures 5 & 6), which is likely linked to clustering of input data as seen in Figure 7. Model rates of exhumation at new locations sampled within the 1000 m contour agree well with the raw exhumation data, despite a significant drop in available data after alignment across all environmental

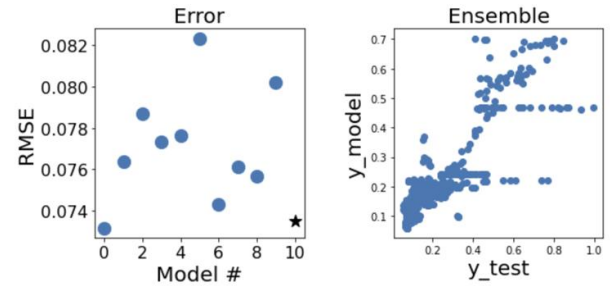


Figure 5. MLP model development and testing results. The black star in the RMSE plot (topleft) indicates RMSE of the ensemble.

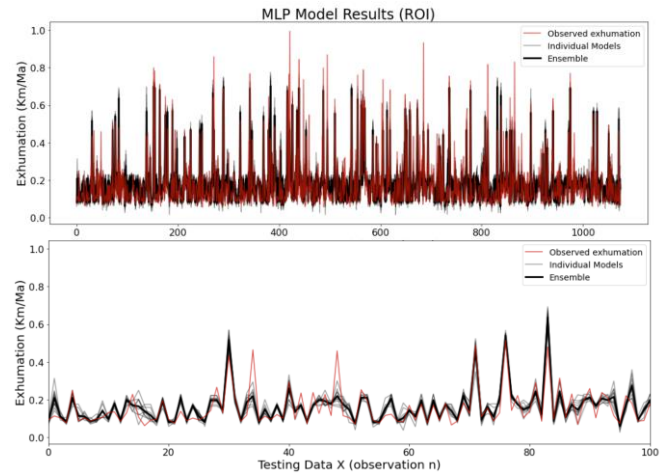


Figure 6. MLP testing data results. Comparison of predicted exhumation by the model ensemble and observed exhumation in out testing dataset. Top displays the entire testing dataset ($n = 1200$) and bottom plots from just 0 to 100 for added detail.

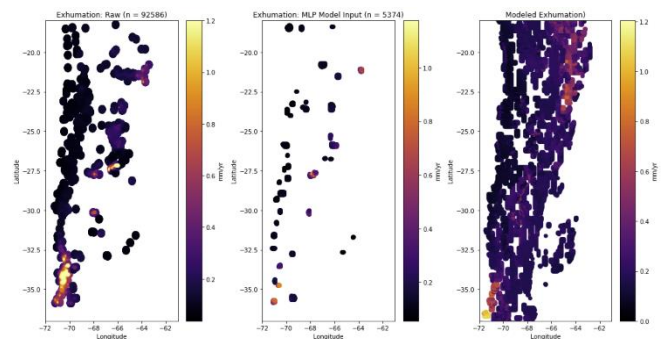


Figure 7. MLP ROI. Raw exhumation data shown on the left, and model input data (middle) where observations for all environmental datasets exist. The right plot shows results of modeled exhumation using the 100 x 100m grid.

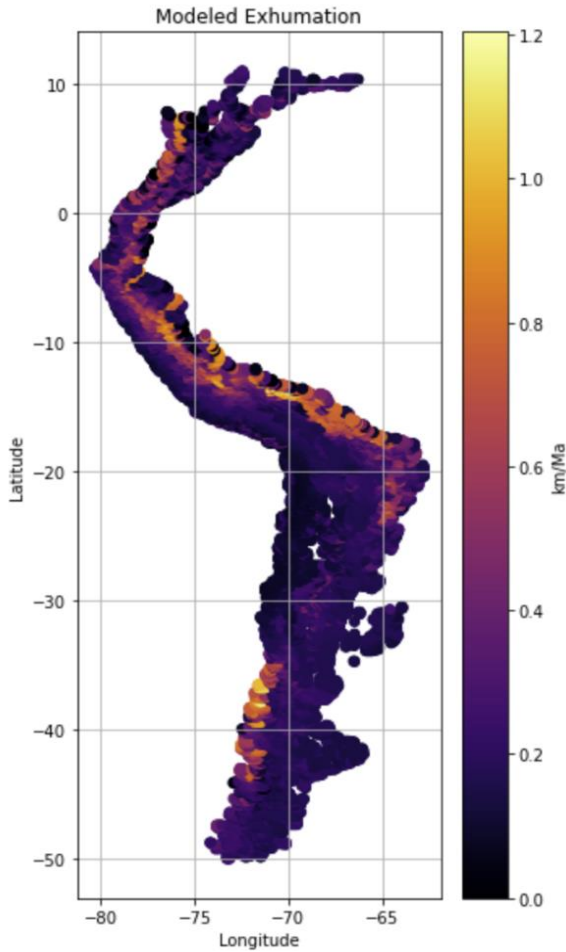


Figure 8. Predicted Exhumation from 10°N to 50°S within the 1000 m contour interval.

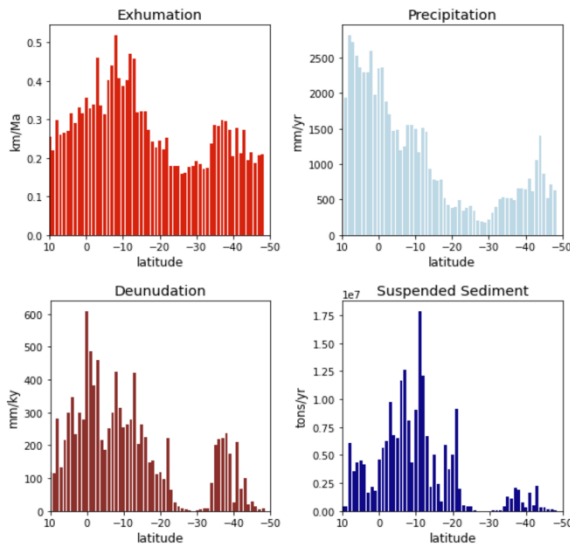


Figure 9. Histogram of variables distribution from 10°N to 50°S. Geology distribution shown in Figure 1.

datasets (Figure 7). It should be noted that highly localized exhumation anomalies may be missed by the model if all environmental datasets were not available at the given sampled location. For example, high rates of exhumation seen in the raw Stadler et al., (2020) data (*e.g.*, at -27.5°S, -66°W) do not appear in modeled results as this area is considered 'no data', despite appearing relatively continuous (Figure 7).

Considering the strong ability to predict exhumation from environmental variables within our testing ROI, the ensemble was used to predict rates of exhumation across the Andes within the 1000 m contour (Figure 8). Modeled exhumation displays unique distribution patterns not shown solely by any one input variables, but influence by weighted input from all controls (Figure 9).

Discussion

Exhumation and denudation share many of the same fundamental drivers, yet their subtle differences in meaning and measurement can provide key insight to regional tectonics and climate controls. As mentioned, the rate of exhumation is the vertical distance traveled by a particular rock in relation to earth's surface over a period of time. Rock will be exhumed by both uplift and faulting processes, but also by surface erosion (Ring et al., 1999). Alternatively, denudation, as calculated in this study, refers to the vertical loss of surface sediments averaged across a watershed and be considered a direct proxy for elevation loss by erosion.

Denudation and exhumation by mechanical weathering is seen to be limited by precipitation in arid/hyper-arid regions of the Andes (Figure 10). The

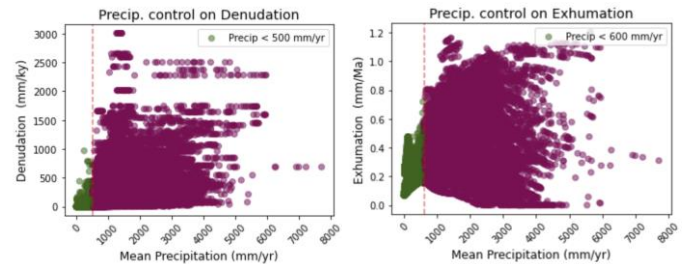


Figure 10. Precipitation control on denudation (left) and exhumation (right). Both variables are limited by precipitation until a threshold of 500 and 600 mm/yr, respectively, is met.

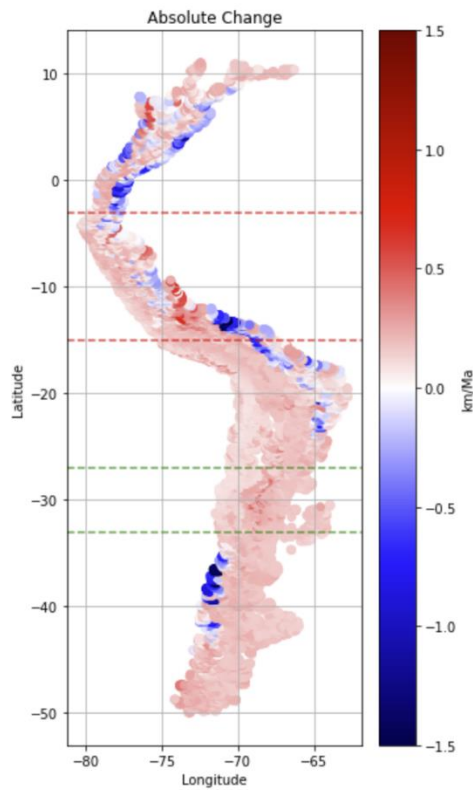


Figure 11. Estimated elevation change by means of exhumation related uplift and elevation loss (i.e. exhumation – denudation). Scale color is adjusted to have a zero at color diverge, where values exceeding this range are plotted as maximum color intensity. Actual range is from -2 to $+0.6$ km/Ma. Red and green dashed lines indicate locations of flat slab subduction.

control on denudation is strong when precipitation is less than 500 mm/year. After reaching this threshold, the influence of precipitation on denudation diminishes, suggesting stronger geologic control such as rates of uplift and topographic relief (Ahnert et al., 1970). These results are markedly consistent with other studies across lithologies (e.g. Thomas et al., 2018; Levenson et al., 2017; Ryab et al., 2014). A similar threshold is seen to exist for rates of exhumation at 600mm/yr of precipitation Figure 9). Erosion by precipitation may have important implications for surface uplift by isostatic rebound as mass is lost and transported to lower elevation basins.

As a proxy for vertical growth of the Andes, estimations of vertical change were calculated by subtracting observed denudation from modeled exhumation. Figure 11 shows calculated vertical change in

kilometers per million years. We would expect regions experiencing larger rates of uplift to show larger positive vertical change. A visual correlation with regions of flat slab subduction in the Andes is evident with continuous elevation gain across horizontal extent in Figure 11. This agrees with studies attributing Andean flat slab subduction, and increased plate coupling, with block fault uplift of the basement core (Gutscher et al, 2000; Alvarado et al., 2009; Espurt et al., 2008). At a localized scale, *trends* of calculated uplift agree with studies focused on the northern Altiplano between $16 - 25^{\circ}\text{S}$ (e.g. Gregory-Wodzicki, 2000; Kober et al., 2015). Gregory-Wodzicki (2000) suggest general rates of uplift between $0.2 - 0.3$ km/Ma since the late Miocene, which agree well with our estimates of this area (Figure 11). Within the eastern most margin of this region, there is a noticeable west to east gradient of increasing absolute change (i.e. uplift) from the Eastern Cordillera and Interandean Zone, to the Subandean Zone. Our results suggest $-0.5 - 0$ km/Ma elevation gain along the Eastern Cordillera and Interandean Zone, and $0.5 - 1.0$ Km/Ma elevation gain along the Eastern Cordillera. These results are close, but slightly underpredict ranges of $0 - 0.2$ km/Ma and $0.5 - 2.0$ Km/Ma suggested by Lamb et al (2002) (as summarized by Kober et al, 2015). Slight underprediction by the model within these ranges was expected from the MLP diagnostic plots (Figures 5 and 6).

Comparing rates of exhumation and denudation with the width of crustal shortening provides insights to the larger tectonic processes of the orogen. Average rates of exhumation and denudation were calculated at 1-degree latitudinal intervals, along with width of the orogen at the 1000 m elevation contour. These measurements are considered orthogonal to strike of the subduction considering the largely north/south direction of the Andes. Averaged rates of exhumation were divided by average observed denudation for each latitudinal bin. High ratio values indicate regions where uplift and surface unroofing (expressed by exhumation) exceeds rates of removal (expressed by denudation). A positive correlation between the exhumation/denudation ratio and width of the Andes is found (Figure 12). One reasonable explanation for this correlation is eastern migration of the orogen into

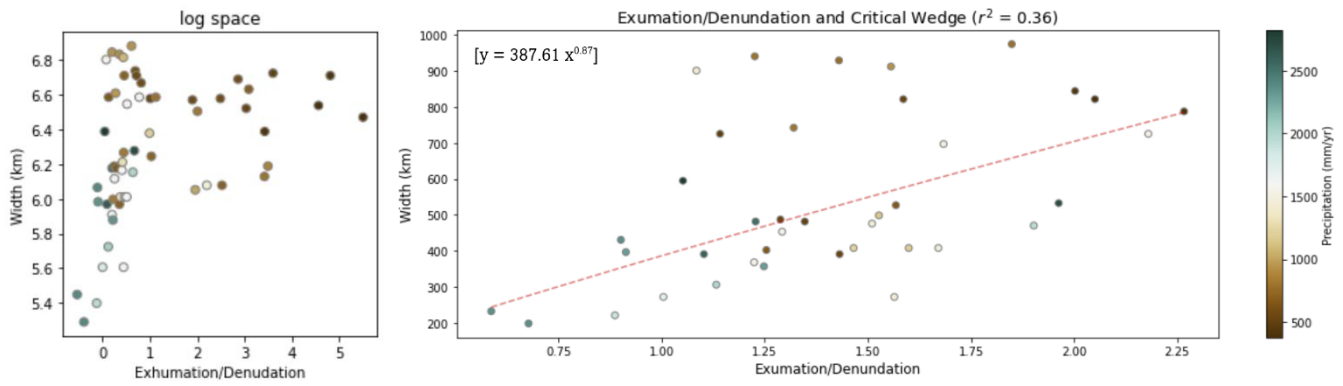


Figure 12. Comparison of the Exhumation/Denudation ratio with width of the Andes. On the left, all data is plotted in log-log space. A power law relation can be seen to exist in the log-log plot. To better analyse the relationship with observations that have not yet leveled off, ratio values less than 2.5 were used in the plot on the right. The trend line is fit by the equation $[y = 387.61 x^{0.87}]$ and has an r^2 of 0.36.

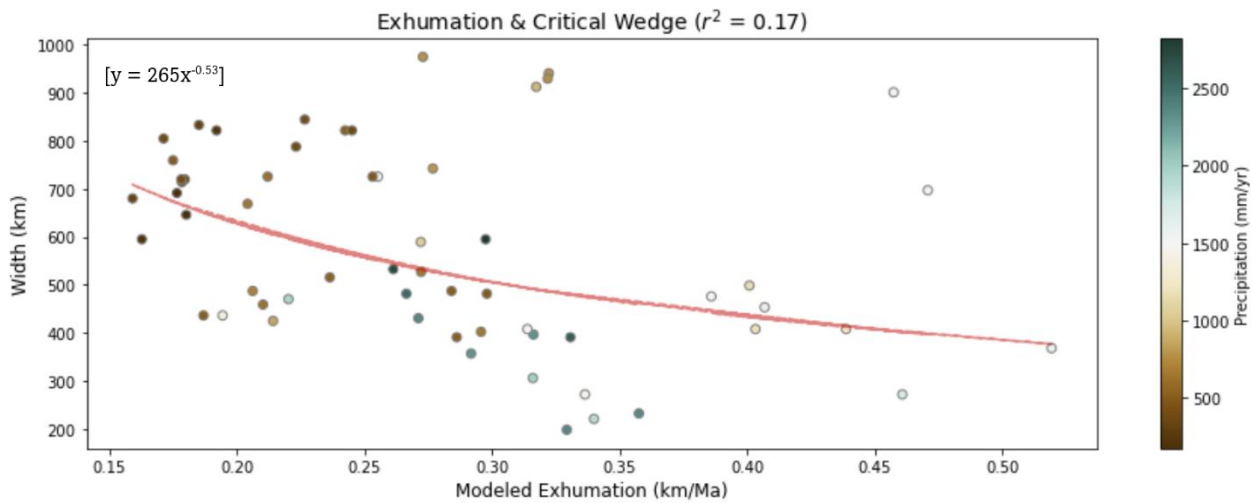


Figure 13. Comparison of Exhumation, a proxy for erosion, with width of the Andes. The trend line is fit by the equation $[y = 265x^{-0.53}]$ and has an r^2 of 0.17.

the foreland by thrusting, as the system works to maintain its critical taper. Vertical growth of the Andes will occur where rates of exhumation exceed rates of denudation i.e. when mass accreted is greater than mass eroded. If an equilibrium with weathering and erosion is not maintained, then the system may fall into a super-critical state, provoking propagation and widening (Simpson, 2006; Strecker et al., 2007). This theory is similarly supported by the negative correlation between modeled exhumation and width of the Andes shown in Figure 13. Latitudes with low average exhumation correspond with increased width of the Andes. While processes of uplift and faulting have strong influence exhumation rates, relations between erosion and exhumation are equally as important. Exhumation can also be considered a proxy

for erosion when observed independently, with exhumation by erosion typically expressed as smooth regional transitions (Ring et al., 1999) (Figure 8). Latitudes with low rates of exhumation, and therefore erosion, will increase their upper surface angle over time, leading to propagation and widening of the basal angle to maintain a critical state, as shown by Figure 13.

Whether analyzing widening of the Andes in terms of exhumation/denudation, or exhumation by erosion, the process occurs most strongly in regions where precipitation is less than 500mm/year (*see colored scatter of Figures 12 and 13*). This relates well with the observed precipitation control on rates of exhumation and denudation shown in Figure 10. It is reasonable to

suggest that areas such as the Altiplano-Puna plateau may not have reached its extensive elevation and width under wetter climate conditions and higher erosion rates.

Conclusion

In this study, we have applied MLP deep-learning techniques to successfully estimate exhumation rates across the Andes mountains from 10°N to 50° at a 100-meter spatial scale. This was done using simple data of precipitation, suspended sediment, catchment area, and geology; environmental datasets which are available globally across diverse tectonic settings. Analysis of model predictions reveal valuable links between climate and tectonics of the Andes such as estimations of surface uplift over the last 2 Ma, and trends between exhumation, precipitation, and horizontal extension of the orogen. While preliminary results seem to generally agree with existing literature, further analysis should be done to validate model results with field studies at local scales as well as expand model training data to include a greater latitudinal extent. In conclusion, machine learning can be used to better constrain the relationships between climate and tectonics, which appear to have strong relations. This enables powerful associations to be drawn and in turn facilitates geologic datasets with spatial resolutions not possible through field work alone. Understanding the impacts of climate variability on large scale mountain building can help geologist better predict how landscapes will evolve under future conditions, or theorize how they have evolved in the past.

Literature Cited

- Ahnert, F., 1970, Functional relationships between denudation, relief, and uplift in large, mid-latitude drainage basins: *American Journal of Science*, v. 268, p. 243–263, doi:[10.2475/ajs.268.3.243](https://doi.org/10.2475/ajs.268.3.243).
- Alvarado, P., Pardo, M., Gilbert, H., Miranda, S., Anderson, M., Saez, M., and Beck, S., 2009, Flat-slab subduction and crustal models for the seismically active Sierras Pampeanas region of Argentina, *in* *Backbone of the Americas: Shallow Subduction, Plateau Uplift, and Ridge and Terrane Collision*, Geological Society of America, doi:[10.1130/2009.1204\(12\)](https://doi.org/10.1130/2009.1204(12)).
- Avouac, J.P., and Burov, E.B., 1996, Erosion as a driving mechanism of intracontinental mountain growth: *Journal of Geophysical Research: Solid Earth*, v. 101, p. 17747–17769, doi:[10.1029/96JB01344](https://doi.org/10.1029/96JB01344).
- Beaumont, C., Fullsack, P., and Hamilton, J., 1992, Erosional control of active compressional orogens, *in* McClay, K.R. ed., *Thrust tectonics*, Dordrecht, Springer Netherlands, p. 1–18, doi:[10.1007/978-94-011-3066-0_1](https://doi.org/10.1007/978-94-011-3066-0_1).
- Compagnucci, R.H., 2011, Atmospheric circulation over Patagonia from the Jurassic to present: a review through proxy data and climatic modelling scenarios: *PATAGONIAN PALAEO-ATMOSPHERIC CIRCULATION: Biological Journal of the Linnean Society*, v. 103, p. 229–249, doi:[10.1111/j.1095-8312.2011.01655.x](https://doi.org/10.1111/j.1095-8312.2011.01655.x).
- Espinoza, J.C., Garreaud, R., Poveda, G., Arias, P.A., Molina-Carpio, J., Masiokas, M., Viale, M., and Scaff, L., 2020, Hydroclimate of the Andes Part I: Main Climatic Features: *Frontiers in Earth Science*, v. 8, p. 64, doi:[10.3389/feart.2020.00064](https://doi.org/10.3389/feart.2020.00064).
- Esput, N., Funicello, F., Martinod, J., Guillaume, B., Regard, V., Faccenna, C., and Brusset, S., 2008, Flat subduction dynamics and deformation of the South American plate: Insights from analog modeling: *FLAT SLAB AND UPPER PLATE DEFORMATION: Tectonics*, v. 27, p. n/a-n/a, doi:[10.1029/2007TC002175](https://doi.org/10.1029/2007TC002175).
- Fagundes, H. de O., Fan, F.M., Dias de Paiva, R.C., Siqueira, V.A., Buarque, D.C., Kornowski, L.W., Laipelt, L., and Collischonn, W., 2020, Sediment flows in South America supported by daily hydrologic-hydrodynamic modeling: *Hydrology preprint*, doi:[10.1002/essoar.10503046.2](https://doi.org/10.1002/essoar.10503046.2).
- Fox, M., Herman, F., Willett, S.D., and May, D.A., 2013, A linear inversion method to infer exhumation rates in space and time from thermochronometric data: *Cross-cutting themes: Geochronology applied to establish timing and rates of Earth surface processes preprint*, doi:[10.5194/esurfd-1-207-2013](https://doi.org/10.5194/esurfd-1-207-2013).
- Garner, H.F., 1959, STRATIGRAPHIC-SEDIMENTARY SIGNIFICANCE OF CONTEMPORARY CLIMATE AND RELIEF IN FOUR REGIONS OF THE ANDES MOUNTAINS: *Geological Society of America Bulletin*, v. 70, p. 1327, doi:[10.1130/0016-7606\(1959\)70\[1327:SSOCCA\]2.0.CO;2](https://doi.org/10.1130/0016-7606(1959)70[1327:SSOCCA]2.0.CO;2).
- GEBCO Bathymetric Compilation Group 2021, 2021, The GEBCO_2021 Grid - a continuous terrain model of the global oceans and land., doi:[10.5285/C6612CBE-50B3-OCFF-E053-6C86ABC09F8F](https://doi.org/10.5285/C6612CBE-50B3-OCFF-E053-6C86ABC09F8F).
- Gregory-Wodzicki, K.M., 2000, Uplift history of the Central and Northern Andes: A review: *Geological Society of America Bulletin*, v. 112, p. 1091–1105, doi:[10.1130/0016-7606\(2000\)112<1091:UHOTCA>2.0.CO;2](https://doi.org/10.1130/0016-7606(2000)112<1091:UHOTCA>2.0.CO;2).

- Gutscher, M.-A., Spakman, W., Bijwaard, H., and Engdahl, E.R., 2000, Geodynamics of flat subduction: Seismicity and tomographic constraints from the Andean margin: *Tectonics*, v. 19, p. 814–833, doi:[10.1029/1999TC001152](https://doi.org/10.1029/1999TC001152).
- Kober, F., Zeilinger, G., Hippe, K., Marc, O., Lendzioch, T., Grischott, R., Christl, M., Kubik, P.W., and Zola, R., 2015, Tectonic and lithological controls on denudation rates in the central Bolivian Andes: *Tectonophysics*, v. 657, p. 230–244, doi:[10.1016/j.tecto.2015.06.037](https://doi.org/10.1016/j.tecto.2015.06.037).
- Lamb, S., 2000, Active deformation in the Bolivian Andes, South America: *Journal of Geophysical Research: Solid Earth*, v. 105, p. 25627–25653, doi:[10.1029/2000JB900187](https://doi.org/10.1029/2000JB900187).
- Lamb, S., and Davis, P., 2003, Cenozoic climate change as a possible cause for the rise of the Andes: *Nature*, v. 425, p. 792–797, doi:[10.1038/nature02049](https://doi.org/10.1038/nature02049).
- Levenson, Y., Ryb, U., and Emmanuel, S., 2017, Comparison of field and laboratory weathering rates in carbonate rocks from an Eastern Mediterranean drainage basin: *Earth and Planetary Science Letters*, v. 465, p. 176–183, doi:[10.1016/j.epsl.2017.02.031](https://doi.org/10.1016/j.epsl.2017.02.031).
- Montgomery, D.R., Balco, G., and Willett, S.D., 2001, Climate, tectonics, and the morphology of the Andes: *Geology*, v. 29, p. 579, doi:[10.1130/0091-7613\(2001\)029<0579:CTATMO>2.0.CO;2](https://doi.org/10.1130/0091-7613(2001)029<0579:CTATMO>2.0.CO;2).
- Morris, G.L., and Fan, J. (Eds.), 1998, *Reservoir sedimentation handbook: design and management of dams, reservoirs, and watersheds for sustainable use*: New York, McGraw-Hill, 1 p.
- NASA, 2018, TRMM (TMPA/3B43) Rainfall Estimate L3 1 month 0.25 degree x 0.25 degree V7;, doi:[10.5067/TRMM/TMPA/MONTH/7](https://doi.org/10.5067/TRMM/TMPA/MONTH/7).
- Peyton, S.L., and Carrapa, B., 2013, An Introduction to Low-temperature Thermochronologic Techniques, Methodology, and Applications, *in* *Application of Structural Methods to Rocky Mountain Hydrocarbon Exploration and Development*, American Association of Petroleum Geologists, doi:[10.1306/13381688St653578](https://doi.org/10.1306/13381688St653578).
- Ring, U., Brandon, M.T., Willett, S.D., and Lister, G.S., 1999, *Exhumation processes*: Geological Society, London, Special Publications, v. 154, p. 1–27, doi:[10.1144/GSL.SP.1999.154.01.01](https://doi.org/10.1144/GSL.SP.1999.154.01.01).
- Ryb, U., Matmon, A., Erel, Y., Haviv, I., Benedetti, L., and Hidy, A.J., 2014, Styles and rates of long-term denudation in carbonate terrains under a Mediterranean to hyper-arid climatic gradient: *Earth and Planetary Science Letters*, v. 406, p. 142–152, doi:[10.1016/j.epsl.2014.09.008](https://doi.org/10.1016/j.epsl.2014.09.008).
- Simpson, G.D.H., 2006, Modelling interactions between fold-thrust belt deformation, foreland flexure and surface mass transport: *Basin Research*, v. 18, p. 125–143, doi:[10.1111/j.1365-2117.2006.00287.x](https://doi.org/10.1111/j.1365-2117.2006.00287.x).
- Stalder, N.F., Herman, F., Fellin, M.G., Coutand, I., Aguilar, G., Reiners, P.W., and Fox, M., 2020, The relationships between tectonics, climate and exhumation in the Central Andes (18–36°S): Evidence from low-temperature thermochronology: *Earth-Science Reviews*, v. 210, p. 103276, doi:[10.1016/j.earscirev.2020.103276](https://doi.org/10.1016/j.earscirev.2020.103276).
- Strecker, M.R., Alonso, R.N., Bookhagen, B., Carrapa, B., Hilley, G.E., Sobel, E.R., and Trauth, M.H., 2007, Tectonics and Climate of the Southern Central Andes: *Annual Review of Earth and Planetary Sciences*, v. 35, p. 747–787, doi:[10.1146/annurev.earth.35.031306.140158](https://doi.org/10.1146/annurev.earth.35.031306.140158).

Thomas, F. et al., 2018, Limited influence of climatic gradients on the denudation of a Mediterranean carbonate landscape: *Geomorphology*, v. 316, p. 44–58, doi:[10.1016/j.geomorph.2018.04.014](https://doi.org/10.1016/j.geomorph.2018.04.014).

United States Geological Survey (USGS), 1999, Maps Showing Geology, Oil and Gas Fields and Geologic Provinces of the South America Region: Open-File Report Open-File Report.

Willett, S.D., 1999, Orogeny and orography: The effects of erosion on the structure of mountain belts: *Journal of Geophysical Research: Solid Earth*, v. 104, p. 28957–28981, doi:[10.1029/1999JB900248](https://doi.org/10.1029/1999JB900248).

Xu, H., Wang, Y., and Xie, S.-P., 2004, Effects of the Andes on Eastern Pacific Climate: A Regional Atmospheric Model Study*: *Journal of Climate*, v. 17, p. 589–602, doi:[10.1175/1520-0442\(2004\)017<0589:EOTAOE>2.0.CO;2](https://doi.org/10.1175/1520-0442(2004)017<0589:EOTAOE>2.0.CO;2).

Appendix A

Geologic Unit symbols and abbreviations as shown in Figure 1 (A). Numerical attribution of the unit for use with the MLP model (B). Geologic Map unit name legend provided by USGS (1999) (C).

A

Geology

GLG

Q
T
APZ
K
J
MCi
pC
U
CmO
TrJ
Mm
PZMZ
PMi
Mv
H2O
PZm
CP
Cv
JK
D
PZ
S
C
Tr
AD
P
OS
Cm
Qv
PZv
Pv
ICE
H2O

1: ['Q'],
 2: ['T'],
 3: ['APZ'],
 4: ['K'],
 5: ['J'],
 6: ['MCi'],
 7: ['pC'],
 8: ['U'],
 9: ['CmO'],
 10: ['TrJ'],
 11: ['Mm'],
 12: ['PZMZ'],
 13: ['PMi'],
 14: ['Mv'],
 16: ['H2O'],
 17: ['PZm'],
 18: ['CP'],
 19: ['Cv'],
 20: ['JK'],
 21: ['D'],
 22: ['PZ'],
 23: ['S'],
 24: ['C'],
 25: ['Tr'],
 26: ['AD'],
 27: ['P'],
 28: ['OS'],
 29: ['Cm'],
 30: ['Qv'],
 31: ['PZv'],
 32: ['Pv'],
 33: ['ICE'],
 34: ['H2O']

B

C

MAP UNITS

Sedimentary Rocks

Q	Quaternary
T	Tertiary
KT	Cretaceous-Tertiary
K	Cretaceous
JK	Jurassic-Cretaceous
J	Jurassic
TrJ	Triassic-Jurassic
Tr	Triassic
MZ	Mesozoic
PZMZ	Paleozoic-Mesozoic
P	Permian
CP	Carboniferous-Permian
C	Carboniferous
D	Devonian
S	Silurian
OS	Ordovician-Silurian
CmO	Cambrian-Ordovician
Cm	Cambrian
AD	Precambrian-Devonian
PZ	Paleozoic
APZ	Precambrian-Paleozoic

Igneous and Metamorphic Rocks

Qv	Quaternary volcanics
Cv	Cretaceous-Tertiary volcanics
Mv	Mesozoic volcanics
Pv	Permian volcanics
PZv	Paleozoic volcanics
MCi	Mesozoic-Cenozoic intrusives
PMi	Paleozoic-Mesozoic intrusives
PZi	Paleozoic intrusives
Km	Cretaceous-Mesozoic metamorphics
Mm	Mesozoic metamorphics
PZm	Paleozoic metamorphics
pC	Precambrian undifferentiated

Other Units

H2O	Water
ICE	Glacial Ice
U	Unmapped Area